

THE OFFICIAL MAGAZINE OF THE OCEANOGRAPHY SOCIETY

# Oceanography

#### CITATION

Garcia-Pineda, O., I. MacDonald, C. Hu, J. Svejksky, M. Hess, D. Dukhovskoy, and S.L. Morey. 2013. Detection of floating oil anomalies from the Deepwater Horizon oil spill with synthetic aperture radar. *Oceanography* 26(2):124–137, <http://dx.doi.org/10.5670/oceanog.2013.38>.

#### DOI

<http://dx.doi.org/10.5670/oceanog.2013.38>

#### COPYRIGHT

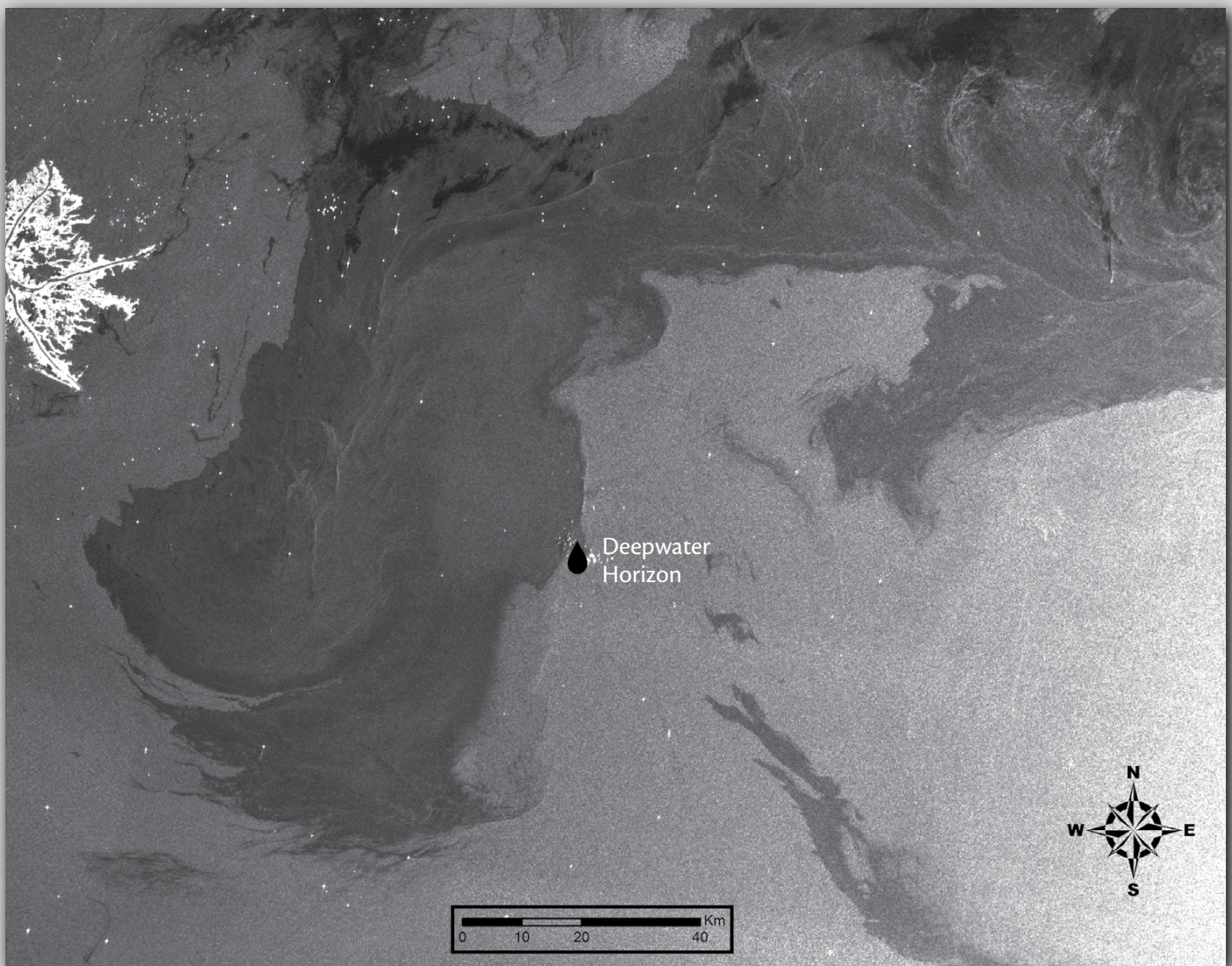
This article has been published in *Oceanography*, Volume 26, Number 2, a quarterly journal of The Oceanography Society. Copyright 2013 by The Oceanography Society. All rights reserved.

#### USAGE

Permission is granted to copy this article for use in teaching and research. Republication, systematic reproduction, or collective redistribution of any portion of this article by photocopy machine, reposting, or other means is permitted only with the approval of The Oceanography Society. Send all correspondence to: [info@tos.org](mailto:info@tos.org) or The Oceanography Society, PO Box 1931, Rockville, MD 20849-1931, USA.

# Detection of Floating Oil Anomalies From the Deepwater Horizon Oil Spill With Synthetic Aperture Radar

BY OSCAR GARCIA-PINEDA, IAN MACDONALD,  
CHUANMIN HU, JAN SVEJKOVSKY, MARK HESS,  
DMITRY DUKHOVSKOY, AND STEVEN L. MOREY



**ABSTRACT.** Detection of oil floating on the ocean surface, and particularly thick layers of it, is crucial for emergency response to oil spills. While detection of oil on the ocean surface is possible under moderate sea-state conditions using a variety of remote-sensing methods, estimation of oil layer thickness is technically challenging. In this paper, we used synthetic aperture radar (SAR) imagery collected during the Deepwater Horizon oil spill and the Texture Classifier Neural Network Algorithm (TCNNA) to identify the spill's extent. We then developed an oil emulsion detection algorithm using TCNNA outputs to enhance the contrast of pixels within the oil slick in order to identify SAR image signatures that may correspond to regions of thick, emulsified oil. These locations were found to be largely consistent with ship-based observations and optical and thermal remote-sensing instrument data. The detection method identifies regions of increased radar backscattering within larger areas of oil-covered water. Detection was dependent on SAR incident angles and SAR beam mode configuration. L-band SAR was found to have the largest window of incidence angles (19–38° off nadir) useful for detecting oil emulsions. C-band SAR showed a narrower window (20–32° off nadir) than L-band, while X-band SAR had the narrowest window (20–31° off nadir). The results suggest that in case of future spills in the ocean, SAR data may be used to identify oil emulsions to help make management decisions.

## INTRODUCTION

The blowout of the Deepwater Horizon (DWH) MC-252 well in the Gulf of Mexico caused the largest accidental offshore oil discharge in history, greater than either the Ixtoc-1 blowout off the coast of Mexico (Jernelöv and Lindén, 1981) or the *Exxon Valdez* spill in Alaska (Xia and Boufadel, 2010). The DWH discharge started on April 20, 2010, with the explosion and sinking of the DWH platform and continued through July 15, when the wellhead was capped. Oil remained on the sea surface for more than 100 days (McNutt et al., 2011). Massive efforts were mobilized in response to this environmental disaster. The contingency activities directed to floating oil included the application of dispersants (by planes or vessels), skimming, booming, and in situ burning. To coordinate these emergency response activities (inshore or offshore), detection and prediction of the state and fate of the oil was a crucial daily task.

During DWH discharge, all available remote-sensing technology was mobilized to support the monitoring efforts. As a result, an unprecedented amount of remote-sensing data was collected. Analyzing and interpreting these data remains a very active area of research that can expand synthetic aperture radar (SAR) oil spill response capabilities (Maurizio et al., 2012; Minchew et al., 2012; Garcia-Pineda et al., 2013). In this paper, we examine SAR anomalies in floating oil discharged from the DWH and consider the evidence that they correspond to regions of oil emulsions within the overall layer.

Assessment of floating oil distribution is a crucial response function for all marine oil spills that depends heavily on remote-sensing data analysis. Some remote-sensing techniques include optical, microwave, and radar sensors that can be set up on both aircraft and satellites (Brekke and Solber, 2005; MacDonald, 2010; Leifer et al.,

2012). In addition to SAR data, visible and near-infrared (NIR) spectra satellite imagery has also been used to delineate surface oil slicks in the ocean (MacDonald et al., 1993). Recently, the wider availability of the Moderate Resolution Imaging Spectroradiometer (MODIS) and MEdium Resolution Imaging Spectrometer (MERIS) data also made it possible to use these wide-swath (2,330 km and 1,150 km, respectively) satellite instruments for cost-effective spill monitoring in near real time (Hu et al., 2003, 2009). However, no single sensor can provide all the information needed for effective oil spill response management; each comes with its own advantages and disadvantages. Satellite remote sensing provides lower temporal and spatial resolution than airborne remote sensing; however, it is cost effective, offers an extensive overview of affected areas, and can be processed more rapidly.

SAR has been widely used to detect the presence or absence of oil slicks (Alpers and Hühnerfuss, 1988; Clemente-Colón and Yan, 2000). Semi-automated routines developed for this purpose employ different image-processing algorithms such as neural networks, adaptive thresholding, and fuzzy logic (Del Frate et al., 2000; Topouzelis et al., 2008; Mera et al., 2012). However, the lack of sea level verification of algorithm results has constrained opportunities for spill classification. For example, natural oil seeps reliably generate layers of floating oil useful for testing the effectiveness of algorithms, but their low discharge rates do not produce very thick oil-emulsion layers (De Beukelaer et al., 2003; Garcia-Pineda et al., 2010). Tanker spills often produce transient targets that are transported to

shore relatively quickly. In this context, the DWH discharge was unique because it generated floating oil layers over a vast area, and spill thickness and weathering history varied. The long duration of the event allowed these features to be imaged repeatedly by SAR and other satellite instruments. Numerical circulation models further helped predict spill trajectories during DWH operations (Liu et al., 2011). The combination of a variety of remote-sensing instruments, such as SAR, MODIS, MERIS, and aerial thermal imagery, provided timely information on the location and size of surface oil slicks (Leifer et al., 2012). However, to date, the most technically challenging aspect of oil spill remote sensing is not detecting oil presence or absence, or oil slick size, but quantifying oil slick thickness or volume (Minchew et al., 2012).

The wide occurrence of thick, emulsified oil during the DWH discharge created opportunities for studying this material in a real-world setting. For example, analysis of Uninhabited Aerial Vehicle Synthetic Aperture Radar (UAVSAR) data by Minchew et al. (2012) showed that SAR can detect oil emulsions as long as the effect on total radar backscatter can be distinguished from

the effect of wave tilt and surface roughness. There was also direct observation and measurement of layer thickness. Targeting of response efforts like burning boom operations and aerial dispersant applications offered additional confirmation of thick oil concentrations. In this study, we attempt to identify oil emulsions with L-, C-, and X-band SAR data using single polarimetric SAR, generally with VV-polarization, as well as other satellite and airborne measurements. We verify these results by comparing them to independently identified regions of thick oil and sea truth sampling of oil emulsions during expeditions led by Florida State University (<http://deepwaterhorizon.fsu.edu/tracking.php>) and Norwegian SINTEF Group (<http://www.sintef.com>) scientists.

## MATERIALS AND METHODS

### Principle of Detecting Floating Oil Using SAR

Radar uses microwave radiation to detect the range, speed, and other characteristics of remote objects (Knott et al., 2004). Active satellite imaging, such as SAR, detects the interaction between different Earth surfaces and microwaves; an image is formed by transiting the antenna along

a fixed path (synthetic aperture). From the full range of microwave frequency bands (Figure 1), most SAR satellites use L-, C-, and X-bands to image land and ocean surfaces. These frequencies have been chosen by satellite operators based on the number of applications they offer and their capability to detect different geophysical processes (Clemente-Colón and Yan, 2000). Three main components dominate the return of energy to a SAR satellite from Earth's surface: (1) the geometry between the relative positions of the satellite and the surface imaged (i.e., directional spectra of waves and beam incidence angles), (2) surface roughness, and (3) the dielectric properties of the surface materials (Alpers and Espedal, 2004).

Over land, the heterogeneity of a SAR image is dominated by energy reflected from the local topography, which is generally highly heterogeneous and highly conductive. For ocean imaging, the energy detected by the SAR antenna is strongly influenced by radar cross section (RCS). As Knott et al. (2004) describe, RCS is a measure of the power scattered in a given direction when a target is illuminated by an incident electromagnetic wave. RCS is normalized to

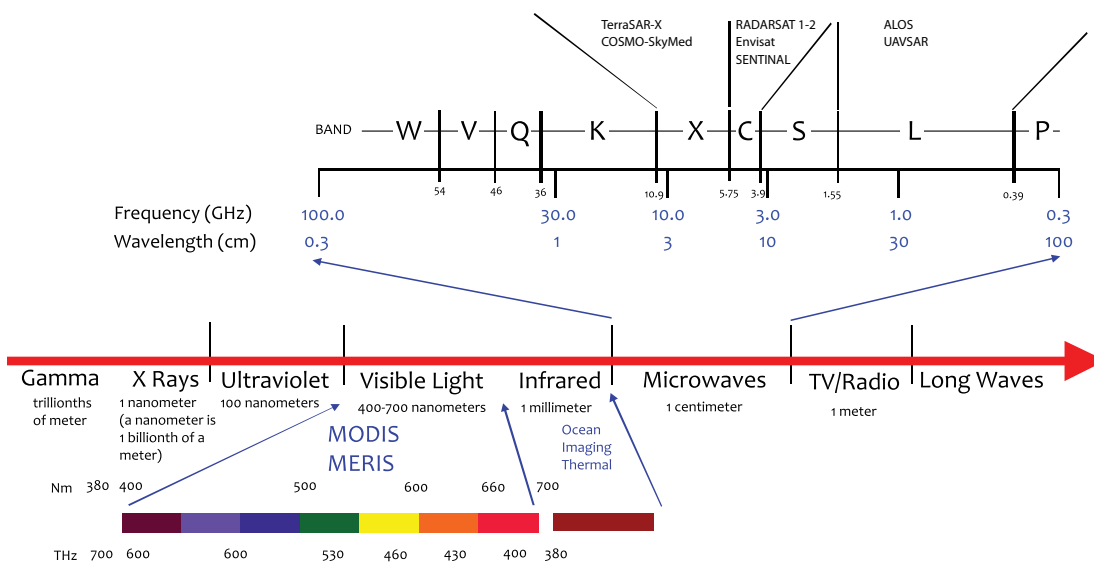


Figure 1. Microwave frequency and wavelength range for synthetic aperture radar (SAR) instruments/satellites. In contrast, optical and infrared satellites and aerial sensors (e.g., MODIS, MERIS, Landsat, and OI Thermal) operate in a narrower range of wavelengths using solar radiation to detect floating oil.

the power density of the incident wave at the target so that it does not depend on the distance of the target from the illumination source. As the energy incident angle increases (with respect to nadir), RCS also increases, and less energy per unit area is reflected back to the satellite (Holt, 2004). This effect produces SAR ocean images with a gradient of decreasing brightness from the near-nadir to the far-nadir sides of the image. As is the case for photography, the normalized RCS (NRCS) derived from SAR depends on the observed scene as well as the conditions of observation, which are affected by the sea surface roughness. RCS is also affected by the specific SAR system configuration, including its frequency, polarization, sensor velocity, pulse repetition frequency and duration, chirp bandwidth, and RCS normalization. An image of the sea surface typically shows local variation in roughness, which is a function of wind waves and swell. Surface oil modulates fine-scale roughness and enhances specular reflection from the seawater surface under the oil. This results in a signal that is locally less intense than that from surrounding oil-free water, thus making the oil slick in SAR imagery appear darker than the water.

The following dispersion equation generally governs physical processes mentioned above:

$$w^2 = gk + \frac{\varphi}{\rho} k^3, \quad (1)$$

where  $w$  is the angular frequency of the ocean wave,  $g$  is the gravity acceleration,  $\varphi$  is the surface tension,  $\rho$  is the water density, and  $k$  is the surface wave number (Valenzuela, 1978; Huehnerfuss et al., 1983). This relationship clearly shows that gravity force governs long waves and swell, in contrast to the very short waves related to surface tension, which are

usually generated by wind (Franceschetti et al., 2002). Swell and wind-driven waves generate tilted, slightly rough facets, which are the primary Bragg scatterer on the ocean's surface. As Minchew et al. (2012) describe, these perturbations produce polarized backscatter from ocean waves of wavenumber

$$k_B = 2k_r \sin\theta, \quad (2)$$

where  $k_r$  is the radar wavenumber and  $\theta$  is the incidence angle. The following gives the radar incidence angle  $\theta_i$  relative to the tilted facet:

$$\theta_i = \cos^{-1}[\cos(\theta + \beta) \cos(\delta)], \quad (3)$$

where  $\beta$  is the angle between the vertical and the projection of the tilted facets normal to the scattering plane, and  $\delta$  is the angle between the vertical and the projection of the tilted facets perpendicular to the scattering plane. The majority of the SAR satellite data collected during the DWH oil spill was available in VV-polarization, which is preferred because larger RCS from the sea surface yields larger differences between the images of oil slicks and non-oiled sea surface (Valenzuela, 1978). The dielectric permittivity of a SAR-imaged surface is a measure of the polarization field induced in the surface's material resulting from the application of an external electric field. The external field is generally time-dependent. At the limit of zero

frequency, the surface's material property  $\epsilon$  is often called the dielectric constant (May et al., 2008). In this regard, the relationship between the VV-polarized Bragg scattering coefficients given by the incidence angle and the dielectric constant of different oil emulsions is

$$R_{vv} = \frac{(\epsilon_r - 1)\{\sin^2(\theta_i) - \epsilon_r[1 + \sin^2(\theta_i)]\}}{(\epsilon_r \cos(\theta_i) + \sqrt{\epsilon_r - \sin^2(\theta_i)})^2}, \quad (4)$$

where  $\epsilon_r$  is the relative dielectric constant of the imaged surface (Minchew et al., 2012). Therefore, the dielectric properties of the surface also influence the SAR ocean image. Seawater has very high conductivity, while oil has low conductivity, and the potential contrasts in Bragg scattering properties should be noted. Floating oil is highly heterogeneous depending on oil type and weathering history (Fingas and Fieldhouse, 2012). Over time, floating oil layers form durable emulsions with seawater (we discuss the characteristics of oil emulsions and their effect on energy return in a later section). Fundamentally, water-in-oil and oil-in-water emulsions (w/o and o/w) have higher conductivity and, hence, a Bragg scattering coefficient that is intermediate between water (very high) and unemulsified oil (very low). We hypothesize that this effect will permit detection of emulsified oil over larger regions of floating oil within a range of SAR incident angles.

---

**Oscar Garcia-Pineda** ([oscar.oggp@gmail.com](mailto:oscar.oggp@gmail.com)) is Research Scientist, Department of Earth, Ocean, and Atmospheric Science, Florida State University, Tallahassee, FL, USA.

**Ian MacDonald** is Professor, Department of Oceanography, Florida State University, Tallahassee, FL, USA. **Chuanmin Hu** is Associate Professor, College of Marine Science, University of South Florida, St. Petersburg, FL, USA. **Jan Svejksky** is President, Ocean Imaging Corporation, Solana Beach, CA, USA. **Mark Hess** is Director of Operations, Ocean Imaging Corporation, Littleton, CO, USA. **Dmitry Dukhovskoy** is Associate Research Scientist, Center for Ocean-Atmosphere Prediction Studies (COAPS), Florida State University, Tallahassee, FL, USA. **Steven L. Morey** is Senior Research Scientist, COAPS, Florida State University, Tallahassee, FL, USA.

A number of techniques have been developed to determine phase fractions, electrical conductivity, or dielectric permittivity of o/w and w/o emulsions (May et al., 2008). The dielectric characterization of DWH oil emulsions is beyond the scope of this paper. Thus, the example presented next is intended as a hypothetical case. Using equation 4, Figure 2 shows the Bragg scattering coefficient as a function of incidence angle for three sea surfaces: (1) unemulsified oil ( $\epsilon_r \sim 2$ ), (2) seawater ( $\epsilon_r = 80$ ), and (3) an oil emulsion ( $\epsilon_r = 40$ ). The values assigned for relative permittivity are theoretical and only for illustrative purposes. This hypothetical relationship suggests that an increment on the dielectric constant of the imaged surface by SAR will produce a direct increment on the Bragg scattering coefficient. It follows that if a region of thin oil contains a patch of emulsified oil, Bragg scattering should be locally stronger. Detection of this contrast would indicate where the patches of emulsified oil were located. It is important to point out that no matter how thick an emulsion is, the backscatter would not support a direct measurement

of emulsified or unemulsified oil thickness, but only the presence or absence of an oil emulsion.

### Detection of Floating Oil Using Optical Remote Sensing

Floating oil layers can also be detected in optical images, especially under certain illumination conditions (Hu et al., 2003, 2009), because oil has different optical properties (absorption, scattering, refraction index) than water and because oil modulation of surface roughness can redistribute specular reflection of sunlight (sunglint). Figure 3 shows a portion of a SAR image collected on May 24, 2010, by the Advanced Land Observing Satellite (ALOS; an L-band SAR) and a red-green-blue image collected by MERIS on the same day two hours earlier. As in SAR images, although the optical contrast in MERIS images between oil slicks and surrounding waters makes detecting the presence or absence of surface oil straightforward, with some a priori knowledge of the spill location, quantifying oil volume or characterizing oil into different thickness classes still remains a significant technical challenge.

Most published works rely on laboratory experimental results to develop classification schemes (Clark et al., 2010; Svejksky et al., 2012), but there are no reports on how to classify the multiband MERIS or MODIS data to differentiate oil thickness. Preliminary analysis showed correlation between oil thickness determined from hyperspectral Airborne Visible/Infrared Imaging Spectrometer (AVIRIS) measurements, using the Clark et al. (2010) algorithm, and MODIS reflectance in the near infrared and shortwave infrared for oil slicks under strong sunglint where all oil slicks show positive contrast against a water background (recent work of author Hu). Under such circumstances, emulsified oil appears brighter than the surrounding thinner oil. When sunglint is negligible, thick oil emulsion also appears brighter than oil sheen in the near-infrared wavelengths. When sunglint shows strong gradients, some oil slicks under relatively weaker sunglint may appear darker than the surrounding water (Hu et al., 2009; Jackson and Alpers, 2010), making it more difficult to differentiate oil thickness classes. In any case, a human analyst is required to interpret optical imagery because there is currently no generalized rule that can be applied blindly to classify oil slicks.

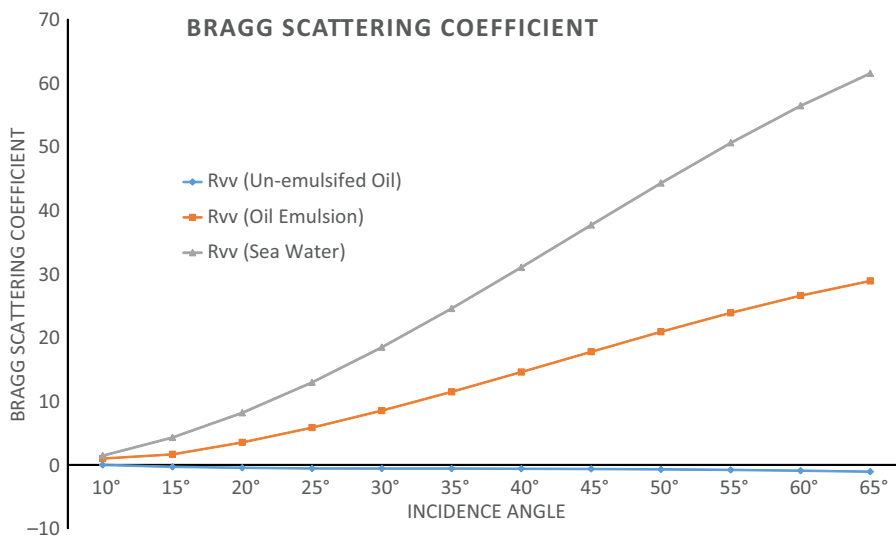


Figure 2. Bragg scattering coefficient for VV-polarization ( $R_{VV}$ ) calculated for three different sea surface conditions covered by: unemulsified oil, emulsified oil, and seawater (Equation 4).

### Weathering of Floating Oil and Effects on SAR Detection

When crude oil is discharged into the ocean, it reacts dynamically with biological, physical, and chemical processes. On the surface, the collective result is known as “weathering” of the oil (Fingas, 2004). Weathering processes include spreading, evaporation, dissolution, dispersion, photochemical oxidation, emulsification, sinking, biodegradation, adsorption to suspended matter, and

deposition onto the seafloor (Fingas and Fieldhouse, 2012).

After spreading, the light volatile components of crude oil begin to evaporate and the remainder begins to emulsify. The rate of evaporation depends upon the vapor pressure and the volatile components present in the crude oil. Previous studies show that oil layer thickness can significantly impact the rate of oil evaporation (Brekke and Solber, 2005). Further, the remaining concentrated portion of crude oil mixes with surface seawater under the influence of wind and wave action to form an emulsion (Thibodeaux et al., 2011). An emulsion may be defined as a colloidal mixture of two immiscible fluids, one being dispersed in the other in the form of droplets (Fingas and Fieldhouse, 2012). For a w/o emulsion, the oil is the continuous phase and, consequently, the electrical conductivity of the emulsion is negligible. For an o/w emulsion, water is the continuous phase and, in seawater, the bulk electrical conductivity of the o/w emulsion is large ( $\sim 10 \text{ S m}^{-1}$ ) compared to pure oil, which is an electric insulator (May et al., 2008).

Oil emulsions may be extremely stable because the water droplets (1–10  $\mu\text{m}$  diameter range) are held in a semirigid structure by asphaltenes, waxes, and resins, or similar components (Fingas and Fieldhouse, 2012). The inclusion of water in the crude oil emulsion is an important step in the weathering process because it increases the volume and viscosity of the emulsion and changes its dielectric constant. Emulsions can also seriously impact coastal activities by creating hazardous conditions and nuisances on the shore (Atlas and Hazen, 2011), so detection of emulsion patches is often a priority in oil spill response. Absorption and Bragg scattering of the SAR electromagnetic pulse responds to variations in

electrical conductivity. Our hypothesis is that due to an increase in electrical conductivity (absolute permittivity) and volumetric scattering, as well as altered surface texture, thick patches of floating emulsions will scatter SAR energy more effectively than a thick layer of fresh unemulsified oil, which would work as an electric insulator, or than a thin layer of unemulsified oil, which normally damps capillary waves and makes the sea surface act as a specular reflector. Similarly, thick patches of pure crude oil (unemulsified) would be undetectable by SAR if saltwater were not mixed with surface oil because surface conductivity would be the same as for a thin layer of oil.

### Algorithm Development

Nearly all SAR applications of oil spill monitoring have relied on visual contrast to detect the presence or absence of

surface oil slicks, based on the principles outlined above (Fingas and Brown, 1997; Clemente-Colón and Yan, 2000; Alpers and Espedal, 2004; Holt, 2004). Various segmentation techniques have been proposed. One of them, the Textural Classifier Neural Network Algorithm (TCNNA), employs a combination of edge detectors and texture statistical descriptors to detect floating oil. This algorithm produces a pixel by pixel delineation of oil slick boundaries, regardless of the local brightness and contrast in the SAR image (Garcia-Pineda et al., 2009, 2013). Using semi-automated TCNNA routines, we processed as geotiffs 454 SAR scenes provided by the National Oceanic and Atmospheric Administration (NOAA), and we selected 172 scenes that imaged oil under the best range of weather conditions. This data set included images collected by satellites

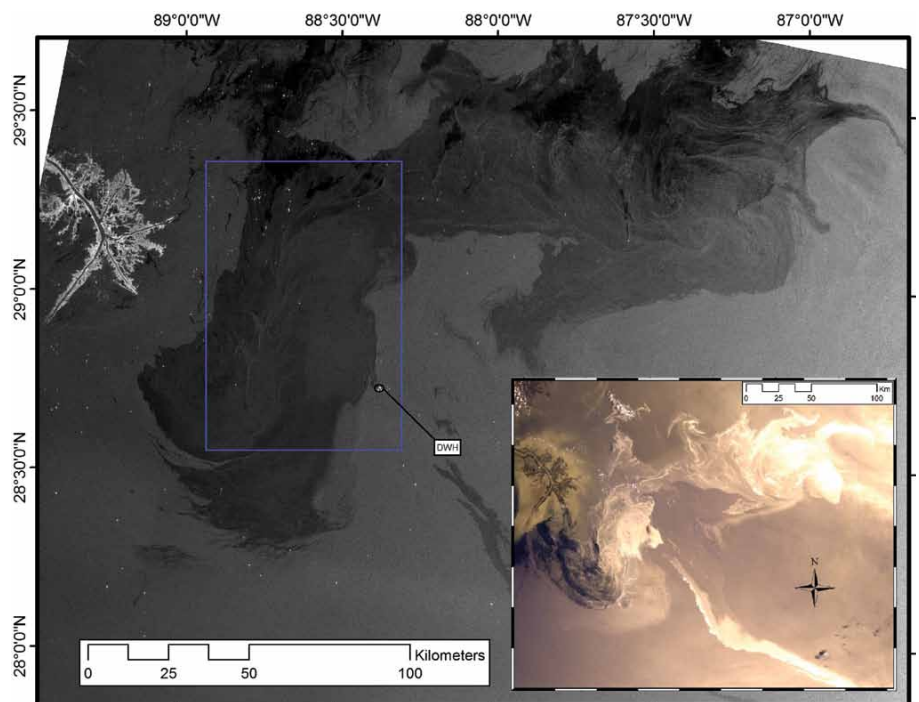


Figure 3. SAR image on May 24, 2010, showing dark features near the Deepwater Horizon oil platform that are thought to be surface oil slicks. Image collected by the Advanced Land Observing Satellite (ALOS, which is L-band). The Mississippi Delta of Louisiana appears on the top left side of the image. The lower right inset shows a red-green-blue (RGB) image collected by MERIS two hours earlier under severe sunglint conditions. An oil slick in optical imagery under sunglint can appear either brighter or darker than the nearby water, depending on the viewing geometry (Hu et al., 2009).

operating in C-, L-, and X-bands in the microwave spectral range from April 25, 2010, to July 12, 2010 (Table 1). To map the spatial coverage of our data set, the 172 TCNNA outputs were intersected and gridded in equidistant 5 km grids.

Using the SAR data set and the delineated surface oil expression maps, we developed a prototype oil emulsion detection algorithm (OEDA).

Each of the delineated oil maps obtained with TCNNA was used to

normalize the effect of the SAR incidence angle and the regional weather conditions. Although the incidence angle and Bragg scattering dependence is well known, we needed to normalize each SAR frame independently to normalize the influence of the regional weather conditions among images captured at different times. Approximately 200 locations outside the oil slick polygon were sampled at different incidence angles for each image (outside the oil boundary defined by TCNNA). As an example, Figure 4 shows the boundary of the oil slick delineated by TCNNA for the SAR image shown in Figure 3. The green squares outside the yellow outline show the locations of sampling pixels and bounding boxes that represent the clean-sea pixels used to normalize the image, as shown below. All pixel values and their relative locations in the image (in reference to the instrument's incidence angle) were stored for two bounding boxes that measured  $25 \times 25$  pixels and  $13 \times 13$  pixels (green boxes in Figure 4). To characterize the textural conditions of the sea surface roughness (produced by local weather conditions) in each of the bounding boxes, we computed four texture descriptors characterizing the average, third moment, entropy, and uniformity of the bounding boxes, as described in Gonzalez et al. (2004). The third moment,

$$\mu = \sum_{i=0}^{L-1} (z_i - m)^3 p(z_i), \quad (5)$$

measures the skewness of the histogram for the NRCS values, where  $\mu$  is the mean (pixel average) intensity,  $z_i$  is the pixel value,  $p(z_i)$  is the histogram of the intensity levels in the bounding box, and  $L$  is the number of possible intensity levels; this measure is 0 for symmetric histograms, positive for histograms skewed to the right (about the mean),

Table 1. Summary of 172 synthetic aperture data sets assessed for oil emulsion detection during the Deepwater Horizon oil spill. A subtotal of 44 images provided results that were suitable for algorithm development.

Band	Satellite	Number of Images	Operating Incidence Angles
C-Band	RADARSAT-1	29	20°–50°
	RADARSAT-2	27	20°–50°
	Envisat	37	15°–45°
	ERS-2	2	20°–26°
X-Band	COSMO-SkyMed	59	20°–59°
	TerraSAR-X	7	20°–45°
L-Band	ALOS	11	18°–43°
<b>Total Number of Images</b>		<b>172</b>	

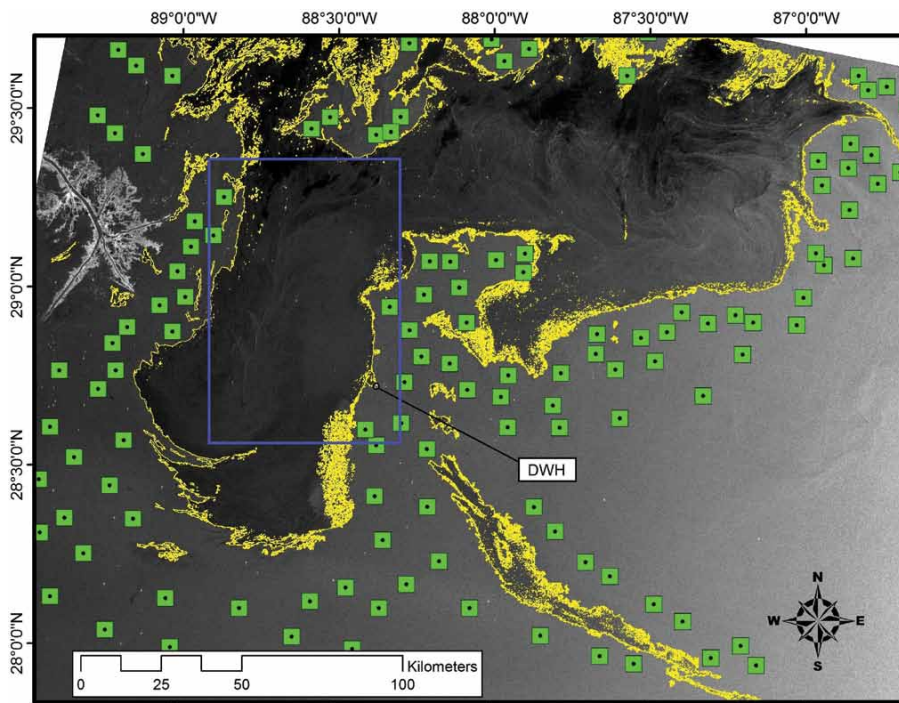


Figure 4. Delineation of oil (yellow) produced by the Texture Classifier Neural Network Algorithm (TCNNA) for the SAR image in Figure 3. Green squares indicate sampling locations of clean-sea pixels and bounding boxes. Bounding boxes are employed to statistically assess regional sea surface roughness conditions using the texture descriptors of Gonzales et al. (2004). The blue box shows the analyzed region reproduced in Figure 6. DWH indicates the location of the Deepwater Horizon oil rig.

and negative for histograms skewed to the left. Entropy derived by

$$e = -\sum_{i=0}^{L-1} p(z_i) \log_2 p(z_i), \quad (6)$$

is a descriptor of the randomness in the bounding boxes around the pixel sampled. Uniformity, derived by

$$U = \sum_{i=0}^{L-1} p^2(z_i), \quad (7)$$

reaches its maximum when all gray levels are equal (maximally uniform) and decreases from there. All the measurements were rescaled to 8 bits (0–255). The mean (pixel average) of the bounding box was then plotted and used to fit a quadratic equation (QE) for all the pixels sampled.

The process explained above was semi-automated and repeated to fit a QE for each of the 172 SAR images in our data set. As expected, the QE varied from SAR image to SAR image because Bragg scattering depends not only on wavelength (C-, L-, or X-band) and incident angle but also on wave tilt and wind conditions (see Figure 5 for an example).

## RESULTS

We confirmed that SAR can distinguish  $R_{VV}$  signatures in portions of certain SAR images by applying OEDA routines. These targets are consistent with what would be expected for detection of floating oil emulsions. The results were also consistent with sea level observations of thick, emulsified oil and suspected detection of emulsions by other sensors. We also confirmed that even using the same beam-mode configuration (same resolution and incidence angle range) on the same satellite, the QE resulting from this normalization needs to be generated for each SAR image because of the different sea state conditions. Figure 5 shows examples of curves fitted for different Envisat SAR images that display oil in

them. Incidence angles of these Envisat images had the same range (from 15° to 45°). The trend lines were generated by sampling pixels under different weather conditions: strong winds (average of 9 m s<sup>-1</sup>, ranging from 5 to 12 m s<sup>-1</sup>), ideal winds (average of 5 m s<sup>-1</sup>, ranging from 4 to 7 m s<sup>-1</sup>), and low winds (average of 3 m s<sup>-1</sup>, ranging from 2 to 8 m s<sup>-1</sup>). Wind values were validated using the Cross-Calibrated Multi-Platform Ocean Surface Wind Vector L3.0 available at <http://podaac-ocpendap.jpl.nasa.gov>. Each beam mode in each satellite produces its own image configuration (pixel resolution, incident angle range); thus, different equalization polynomials are required for different beam modes as well.

The clean-pixel-derived QE was applied to the TCNNA-determined oil pixels to generate a new normalized Bragg scattering raster image, which was then stretched using a second standard deviation function to

increase the image contrast. Next, we used OEDA to more clearly observe the oil emulsions and other signatures inside the oil slick. Figure 6 shows an example before (Figure 6A) and after (Figure 6B) processing for the May 24, 2010, image. Oil emulsions look much brighter and exhibit higher contrast after this treatment.

Using the OEDA outputs, SAR signatures interpreted as oil emulsions were converted to polygons in GIS software. The classified oil emulsion polygons were compared with concurrent (same day) thermal and optical imagery and aerial photography. All of the 172 SAR images were processed independently to obtain the OEDA output. Only 44 SAR images produced features that could be interpreted visually as oil emulsions similar to the example given above. Images with interpreted oil emulsions had low uniformity values (equation 7) and high values for entropy and third moment

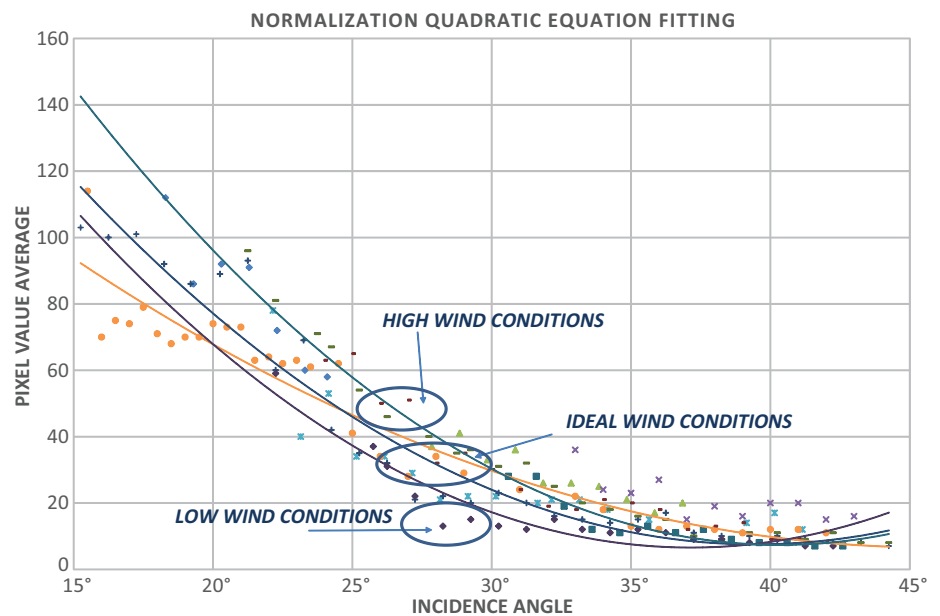


Figure 5. Examples of trend lines for equations fitted for “clean sea pixels” outside the oil slicks sampled from 11 SAR images with the full range of wind conditions collected by the C-Band SAR satellite Envisat during DWH operations. The horizontal axis represents the incident angle in the SAR image, while the vertical axis is the average pixel value in the bounding box.  $R_{VV}$  = Bragg scattering coefficient. o/w = oil in water.

(equations 5 and 6) in the  $25 \times 25$ -pixel bounding boxes. This result suggests that images with more uniformly distributed Bragg scattering (pixel values) in larger areas are less likely to allow detection of signatures inside the oil. SAR images that contain intense speckle and higher variance on the pixel value distribution are more likely to allow detection of oil emulsions.

The flattening and contrast enhancement achieved by this image processing approach produced a new normalized and stretched raster. The assumption is that increasingly higher pixel values in the new raster correspond to increasingly thicker emulsions based on the following hypothesis: if oil is mixed with seawater and it weathers, creating an emulsion, the seawater will increase the effective absolute conductivity of the emulsion (with respect to surrounding unmixed oil) because the dielectric constant of unemulsified oil is much lower than that of emulsified oil. Following this assumption, we threshold the brightest pixels in the new normalized and stretched OEDA raster to classify higher backscatter (with higher concentrations of oil emulsion) features. Various

threshold values could be determined from trial and error to assign relative oil emulsion concentration classes within the oil slick. We assigned different threshold values based on the signatures observed in aerial (thermal data and photography) and satellite imagery.

### Comparison to Optical Remote-Sensing Imagery

OEDA results from the SAR imagery were compared to optical and thermal remote-sensing imagery under different wind conditions. Figure 7A shows a subset of a SAR image collected by RADARSAT-2 (C-Band) on May 10, 2010, at 23:53 UTC. A MODIS optical image (Figure 7B) was collected on the same day at 16:35 UTC, approximately seven hours before the SAR snapshot. The normalization of the SAR data by OEDA (Figure 7C) was downscaled to match the same pixel resolution as MODIS, and then was used to threshold pixel value intensities as shown in Figure 7D. Comparing the OEDA output with the optical image, we observed relative overall agreement in the directionality and size of the signatures detected by the two different sensors that are

thought to be thick oil emulsions, as well as some discordance in the observed signatures. In order to visually compare the two images, we assigned four cutoffs to the new raster pixel intensities, as represented in a red-yellow color map in Figure 7D. The brightest pixels in MODIS generally agree with the upper threshold pixels of the OEDA output (red areas on Figure 7D). These features identified similarly in both sensors suggest that some of these signatures might correspond to layers of thick, unemulsified and emulsified oil. The time gap between the two image acquisitions also affected the relative position of the thick oil detected. Moreover, to quantify the agreement and disagreement between signatures observed by both RADARSAT-2 and MODIS, we randomly projected 206 points on a rectangular area covering the oil slick (Figure 8). MODIS data are shown in the background, and the oil slick extent delineated by TCNNA on the RADARSAT-2 image is outlined in red. We then visually confirmed whether each of the points fell within clean seawater, within the oil slicks, and/or within a region of thick oil emulsions detected by either MODIS or OEDA. We evaluated

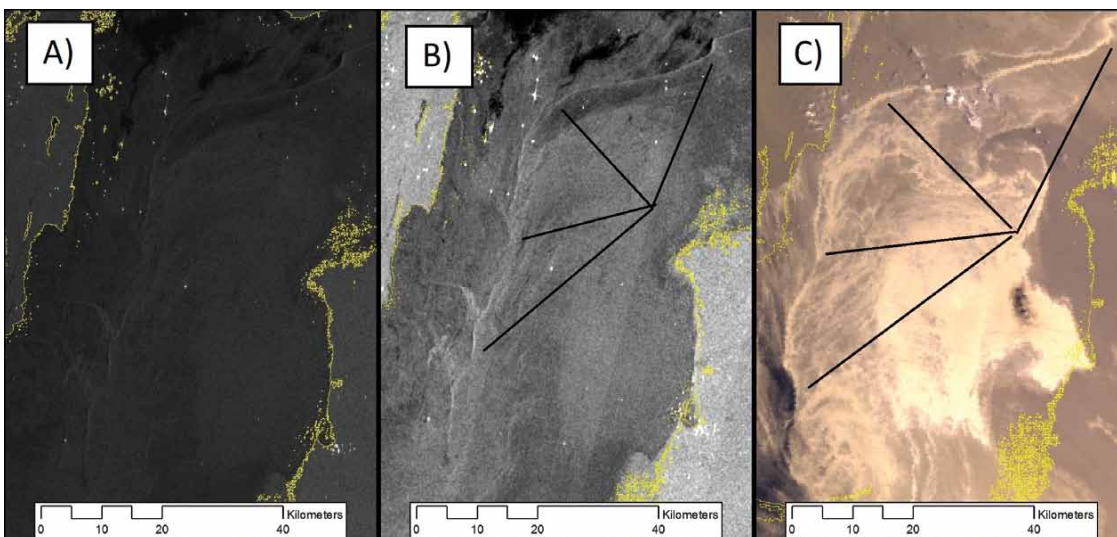


Figure 6. Oil slick delineation (A) bounded by yellow outline and (B) QE normalization for the same SAR image shown in Figure 3. The image collected by MERIS (C) approximately two hours earlier than the SAR image shows similar patterns and signatures made by oil features that are thought to be thick patches of oil emulsions. The feature followed by the black lines in B and C concur on location, shape, size, and orientation to the data collected by the two satellites.

the accuracy of the two observations with a confusion matrix (Lewis and Brown 2001); Table 2 summarizes the results.

We observed that the number of points located inside the oil extent delineated by TCNNA is higher. By visually comparing the red outline (TCNNA from RADARSAT-2) with the MODIS background, we determined that during the approximately six hours between the two acquisitions, the oil slick extended northward and eastward, increasing its area. We quantified 60 points located inside the boundaries of oil emulsions detected by OEDA versus 54 observed in areas where MODIS had the brightest pixel values. From this subset of 54 thick oil sampled points from MODIS, only 37 points (68% of the 54) concurrently fell inside interpreted thick oil or oil

emulsion areas for both satellite images. We performed a Spearman correlation analysis to calculate the statistical dependence between the two variables. We calculated a rank correlation coefficient of 0.71 with a corresponding p-value of .0013, which confirms a significant correlation between the two observations.

#### Comparison of Thermal Remote-Sensing Imagery From Aerial Overflights

During the DWH spill, Ocean Imaging Corp. (OI) conducted daily oil mapping flights over selected portions of the spill with the company's multispectral aerial imager. The instrument had five channels spanning the visible to near-IR thermal range, and was used to quantify probable oil thickness distributions to aid various

response activities (Svejkovsky et al., 2012). In the thermal IR range, both unemulsified and emulsified oil appear cooler than surrounding water when relatively thin, and warmer than surrounding water when very thick. The probable reason for this is that during daytime, the thick oil film absorbs and re-emits solar heat. The positive thermal contrast thus increases with increasing oil thickness. In the case of oil emulsions (Figure 9), their water content reduces the thermal contrast effect so that emulsions with a water content of 50–60% require a thickness of 10 to 15 times that of pure crude oil to exhibit the same thermal contrast magnitude (Svejkovsky et al., 2012). Emulsified oil targets having sufficient thickness to exhibit a positive thermal contrast of 4–5°C or more were imaged relative

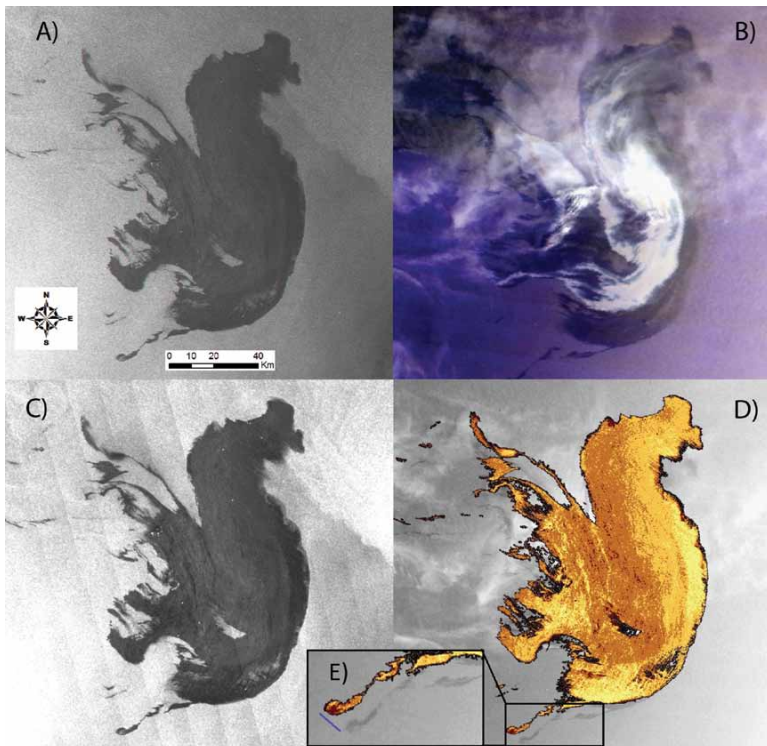


Figure 7. Comparison between (A) a RADARSAT-2 (C-Band) image collected on May 10, 2010, at 23:53 UTC, and (B) a MODIS image collected the same day at 16:50 UTC, showing the various oil contrasts under thin clouds. The image was generated as an RGB composite. The bright features are thought to be from emulsified thick oil, while the dark features are thought to result from thinner oil films. (C) The same SAR image normalized to incident angle. (D) Oil emulsion detection algorithm (OEDA) classification output. A 6 km displacement was observed between the two satellite images (blue line in E).

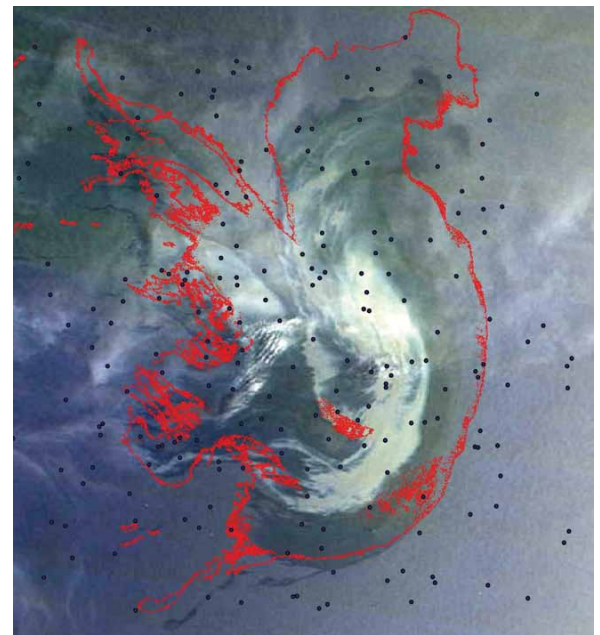


Figure 8. Location of randomly generated points for qualitative evaluation of significance between OEDA and MODIS.

Table 2. Results on the visual interpretation of the 206 sampled points.

	Oil	Water	Thick Oil
TCNNA on RADARSAT-2	107	99	60
MODIS	101	105	54

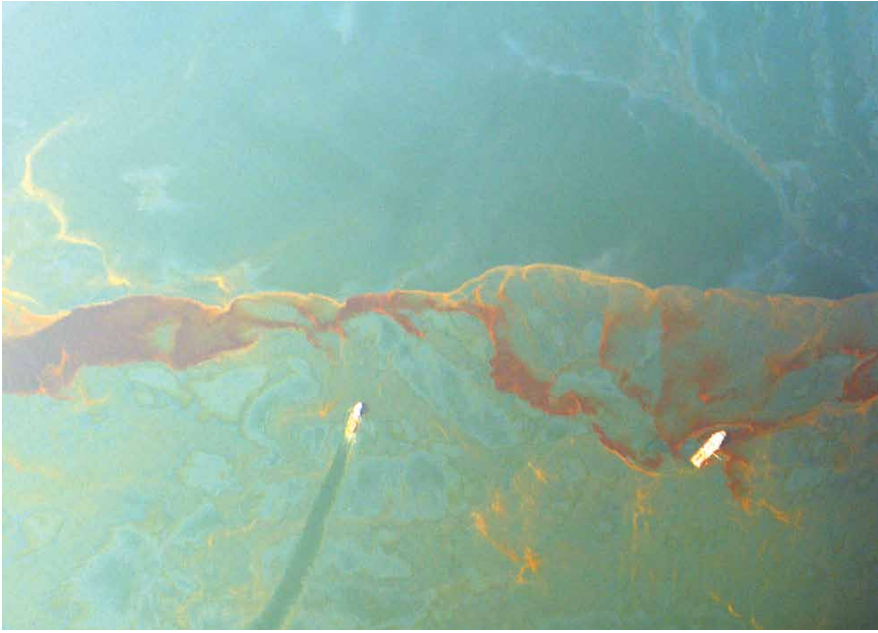


Figure 9. Part of a thick emulsion feature photographed by Ocean Imaging Corporation on June 8, 2010, that exhibited a positive thermal contrast of several degrees Celsius compared to surrounding water when imaged with a thermal IR camera as shown in Figure 10. Two ships (bright white) can be seen in the image.

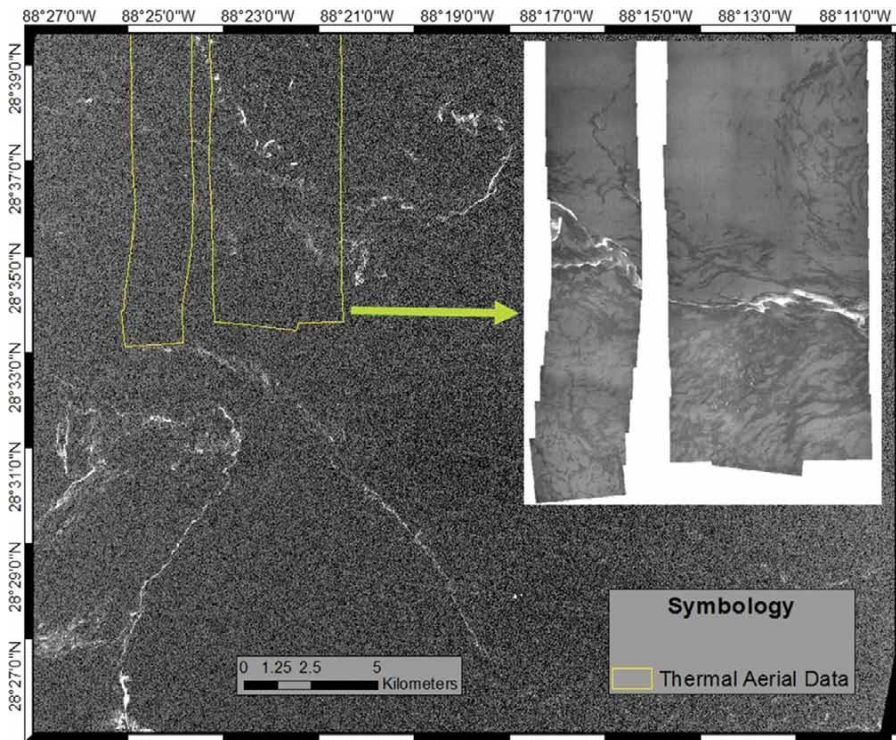


Figure 10. Ocean Imaging Corp's thermal imagery (inset on right) showing hot (white) elongated features corresponding to strands of thick oil emulsions. The TerraSAR-X image (main large image) of the same area was acquired on the same day. The SAR image reveals similar features of high (white) backscatter return. Dark signatures on the thermal image are thought to be thick unemulsified oil.

frequently during OI flights. Ship-based sampling of some of these (usually elongated) emulsion patches revealed thicknesses up to several centimeters and water content in the 40–60% range (Belore et al., 2011). Figure 9 shows an oblique photograph of thick, emulsified oil taken by OI on June 8, 2010, where core areas exhibited a 3–5°C positive thermal contrast in the aerial thermal IR imagery on June 8, 2010 (so thermal contrast is also visible in the optical images). Figure 10 shows the thermal data overlaid on a very-high-resolution (~ 3 m) TerraSAR-X image acquired two hours after the OI aerial imaging on June 8, 2010, at 11:51 UTC. The SAR data show elongated features with high backscatter return signals that correspond closely in location, shape, and size to the high-temperature thick emulsion features noted in the thermal OI data. This coincidence suggests that the SAR-sensed features also correspond to the probable thick emulsions. As described at Svejksky et al. (2012), the dark features observed on OI thermal data collected over the oil spill (Figure 10 inset) represent fresh oil untreated by aerial dispersants; the white signatures correspond to warm patches of thick oil emulsions.

Analysis of the 44 OEDA outputs that detected signatures thought to be oil emulsions shows that each of the SAR L-, C-, and X-bands appeared to be geometrically constrained by the incidence angles within which oil emulsions could be detected. Preliminary results show that L-band SAR images have the largest window of incidence angles (between 19° and 38° off nadir) that could allow detection of oil emulsions. C-band SAR images were found to have a narrower window for oil emulsion detection (between 20° and 32° off nadir) than L-band. The X-band SAR had the

narrowest detection window (between 20° and 31° off nadir). One possible explanation is that SAR wavelength is directly proportional to the radar's penetration depth: longer L-band waves penetrate farther into a medium than shorter waves of C-band and X-band (Knott et al., 2004). However, our method could only be applied to a subset of the total available data (44 images from 172). This suggests that other factors (e.g., wind direction, polarization, oil in water emulsion ratio) may be limiting these ranges as well. SAR image calibration could also have a strong effect by reducing the radiometric resolution.

## DISCUSSION

While oil presence or absence on the ocean surface is relatively easy to delineate with use of semi-supervised processing of SAR imagery, estimating oil thickness is more challenging. Sea level observation/validation remains the most conclusive method, but it is not practical over large areas. One remote-sensing approach is based on measuring thermal energy by IR sensors. Oil absorbs solar radiation differently from the ambient ocean and re-emits a portion of this energy as long-wave radiation in the infrared spectral band. Early studies report that IR sensors observe thick oil as hot spots, intermediate thick oil as cool, while thin oil is not detectable (Fingas and Brown, 1997). Some preliminary results were obtained by using airborne measurements (e.g., Svejkovsky et al., 2012) that partially covered the extent of the slick along respective flight paths. A second approach relied on optical satellite imagery. The approach presented here demonstrates the potential of using SAR imagery for qualitative classification through examining variations of Bragg scattering due to changes in the

conductivity and surface roughness of oil emulsions. Agreement among the results obtained with these techniques was encouraging, but not perfect.

There are several possible explanations for the agreements and discrepancies we observed. Thermal and optical imagery is sensitive to oil thickness, while SAR might only be sensitive to the presence or absence of oil emulsions (regardless of thickness). Another possible reason for the disagreement could be the single polarization used in many of the available SAR images. It is possible that by using fully polarimetric SAR, the agreement between optical and thermal observations and SAR images could be improved.

The most likely cause of the structural characteristics delineated by OEDA was in the effect of emulsion formation and floating volume (i.e., thickness). Although this cannot be definitively verified over the entire areas of the images analyzed, it was possible to ground truth the OEDA anomalies where focused aerial dispersant missions and burning operations targeted thick oil layers based on direct responder observations. Figure 11 shows samples of oil emulsions collected during an expedition conducted by SINTEF in proximity to the DWH wellhead. The purpose of this

sampling expedition was to identify slicks at different stages of weathering using spotter aircraft as well as surface sampling and physical characterization of emulsions from the slicks. The case reported here corresponds to a layer of emulsified oil sampled on June 3, 2010, approximately 12 nautical miles north of the DWH site. Based on visual inspections of the adsorbent pad samples made by SINTEF (SINTEF cruise report A16062), the thickness was approximately 2–4 mm. The emulsion was light brown/orange/reddish in color and appeared more elastic and less prone to spreading on the sea surface, which indicates that this slick had been heavily weathered (evaporative loss, emulsification, and photo-oxidation).

The availability of optical or thermal imagery approximately concurrent in time with OEDA outputs offers a unique opportunity to explore OEDA algorithm performance at different incidence angles and wind conditions. As expected, when different sensors collect two images at nearly the same time, greater agreement on locations of thick oil emulsion signatures can be observed. Qualitative agreement was found for 44 SAR scenes and oil distribution signatures and patterns observed in optical imagery from



Figure 11. Oil film thickness sampling on June 3, 2010, using adsorption pads both for visual estimates and later for quantifying the amount of emulsion adsorbed to the pad in the SINTEF laboratory. Image courtesy of SINTEF (<http://www.sintef.com>)

MODIS, MERIS, Landsat, and airborne thermal and optical imagery. Differences in size and distribution of classified thick oil patches could be due to the time gap between image acquisitions, the presence of unemulsified thick oil (undetectable by SAR), or other geophysical constraints for each sensor (e.g., sunglint, wind, polarization). Lab experiments currently underway at Florida State University will investigate the combined effect of wavelength and incident angle for detection of oil emulsions.

Overall, OEDA shows good potential for identification of thick patches of floating oil for feature tracking and modeling efforts. In addition, the OEDA algorithm may offer valuable applications for many oil spill response operations. For example, the ability to classify thick patches of oil emulsion can result in more effective targeting for skimming or burning operations. These operations typically require the knowledge of both oil presence and quantity and the oil's trajectory in the ocean. Feature identification from SAR has important applications for oil spill trajectory modeling. The resulting maps provide important initial condition and validation data for these models. Typical oil spill models, in their simplest implementations, simulate the movement of oil on the ocean surface by tracking the movement of a large number of particles traveling at a velocity that is some combination of the ocean surface velocity and possibly surface wind (Salem and Kafatos 2001). Particles can initially be placed in the domain based on maps of surface oil slicks, and additional particles can be added to the surface to simulate leaking oil. Although oil is a fluid, its treatment as discrete particles implies that each particle is representative of a certain quantity of oil. This requires knowledge (or often gross estimates) of the amount of oil

reaching the surface from a leaking vessel or subsurface blowout, or of the thickness of the oil covering a given area. For example, if it is assumed that the mean thickness of an oil slick is one micron and each particle represents  $1 \text{ m}^3$  of oil on the surface, then each particle would represent an oil slick of area of  $1 \text{ km}^2$ . However, the thickness of an oil slick is definitely not uniform, and the thickness of a certain quantity of oil may change over time through spreading, emulsification, or other processes. Thus, OEDA can be useful for tracking the thickness of a quantity of oil represented by a discrete particle. Not only is the thickness of an oil slick important for interpreting simulated discrete particles as a surface oil slick, but oil thickness may also have implications for the dynamics of the oil spill. OEDA outputs can be very useful because oil drift models that are able to simulate oil thickness need to be initialized with oil thickness distribution inside the oil spill. This information incorporated into initial fields will improve numerical predictions.

## CONCLUSION

The operating premise for OEDA development is that there are radar backscatter differences between emulsified and unemulsified oil due to an increment in absolute conductivity. Compared with different thicknesses of layers of unemulsified oil, oil emulsions have greater surface roughness and different electrical conductivity due to weathering processes. Therefore, given appropriate weather and instrument conditions, SAR satellites can detect regions of floating oil emulsions. It is important to point out that each beam mode in each satellite produces its own image configuration (pixel resolution, incident angle range), and therefore different equalization polynomials

are needed for different beam modes. Further versions of the OEDA model need to incorporate wind and wave information to produce more accurate normalization and thresholding for oil emulsion detection. Nevertheless, the limited examples shown here, although preliminary in nature, demonstrate the potential of using SAR for classifying thick oil emulsions in the ocean environment.

## ACKNOWLEDGEMENTS

We would like to acknowledge financial support from the Bureau of Ocean Energy Management (BOEM, contract M12PC00003), the BP Gulf of Mexico Research Initiative, and the National Aeronautics and Space Administration (NASA) Ocean Biology and Biogeochemistry Program. We thank the National Oceanic and Atmospheric Administration for providing the SAR imagery and NASA and the US Geological Survey for providing MODIS data. We would also like to thank Stratus Consulting and the NOAA Assessment and Restoration Division for supporting this project. We acknowledge the extensive and critical comments provided by anonymous reviewers that helped to improve this manuscript. 

## REFERENCES

- Alpers, W., and H. Espedal. 2004. Oils and surfactants. Pp. 263–267 in *Synthetic Aperture Radar Marine User's Manual*. C. Jackson and J. Apel, eds, US Department of Commerce, NOAA. Available online at: [http://www.sarusersmanual.com/ManualPDF/NOAASARManual\\_CH11\\_pg263-276.pdf](http://www.sarusersmanual.com/ManualPDF/NOAASARManual_CH11_pg263-276.pdf) (accessed August 26, 2013).
- Alpers, W., and H. Hühnerfuss. 1988. Radar signatures of oil films floating on the sea surface and the Marangoni effect. *Journal of Geophysical Research* 93(C4):3,642–3,648, <http://dx.doi.org/10.1029/JC093iC04p03642>.
- Atlas, R.M., and T.C. Hazen. 2011. Oil biodegradation and bioremediation: A tale of the two worst spills in US history. *Environmental Science & Technology* 45(16):6,709–6,715, <http://dx.doi.org/10.1021/es2013227>.
- Belore, R., K. Trudel, and J. Morrison. 2011. Weathering, emulsification, and chemical dispersibility of Mississippi Canyon 252 crude

- oil: Field and laboratory studies. *Proceedings of the International Oil Spill Conference 2011*, Portland, OR. Available online at: <http://ioscproceedings.org/doi/pdf/10.7901/2169-3358-2011-1-247> (accessed August 26, 2013).
- Brekke, C., and H. Solber. 2005. Oil spill detection by satellite remote sensing. *Remote Sensing of Environment* 95:1–13.
- Clark, R.N., G.A. Swayze, I. Leifer, K.E. Livo, S. Lundeen, M. Eastwood, R.O. Green, R. Kokaly, T. Hoefen, C. Sarture, and others. 2010. *A Method for Qualitative Mapping of Thick Oil Spills Using Imaging Spectroscopy*. USGS Open-File Report 2010-1101. Available online at: <http://pubs.usgs.gov/of/2010/1101> (accessed August 26, 2013).
- Clemente-Colón, P., and X.-H. Yan. 2000. Low-backscatter ocean features in synthetic aperture radar imagery. *Johns Hopkins APL Technical Digest* 21(1):1–6. Available online at: <http://www.jhuapl.edu/techdigest/TD/t2101/clemente.pdf> (accessed August 26, 2013).
- De Beukelaer, S.M., I.R. MacDonald, N.L. Guinasso Jr., and J.A. Murray. 2003. Distinct side-scan sonar, RADARSAT SAR, and acoustic profiler signatures of gas and oil seeps on the Gulf of Mexico slope. *Geo-Marine Letters* 23:177–186, <http://dx.doi.org/10.1007/s00367-003-0139-9>.
- Del Frate, F., A. Petrocchi, J. Lichtenegger, and G. Calabresi. 2000. Neural networks for oil spill detection using ERS-SAR data. *IEEE Transactions on Geoscience and Remote Sensing* 38(5):2,282–2,287, <http://dx.doi.org/10.1109/36.868885>.
- Fingas, M.F. 2004. Preface. *Journal of Hazardous Materials* 107:1, <http://dx.doi.org/10.1016/j.jhazmat.2003.11.005>.
- Fingas, M.F., and C.E. Brown. 1997. Review of oil spill remote sensing. *Spill Science & Technology Bulletin* 4(4):199–208, [http://dx.doi.org/10.1016/S1353-2561\(98\)00023-1](http://dx.doi.org/10.1016/S1353-2561(98)00023-1).
- Fingas, M., and B. Fieldhouse. 2012. Studies on water-in-oil products from crude oils and petroleum products. *Marine Pollution Bulletin* 64(2):272–283, <http://dx.doi.org/10.1016/j.marpolbul.2011.11.019>.
- Franceschetti, G., A. Iodice, D. Riccio, G. Ruello, and R. Siviero. 2002. SAR raw signal simulation of oil slicks in ocean environments. *IEEE Transactions on Geoscience and Remote Sensing* 40(9):1,935–1,949, <http://dx.doi.org/10.1109/TGRS.2002.803798>.
- Garcia-Pineda, O., I.R. MacDonald, X. Li, C.R. Jackson, and W.G. Pichel. 2013. Oil spill mapping and measurement in the Gulf of Mexico with Textural Classifier Neural Network Algorithm (TCNNA). *IEEE Journal of Selected Topics in Applied Earth Observations and Remote Sensing* IEEE PP(99):1–9, <http://dx.doi.org/10.1109/JSTARS.2013.2244061>.
- Garcia-Pineda, O., I. MacDonald, B. Zimmer, B. Shedd, and H. Roberts. 2010. Remote-sensing evaluation of geophysical anomaly sites in the Outer Continental Slope, northern Gulf of Mexico. *Deep Sea Research Part II* 57:1,859–1,869, <http://dx.doi.org/10.1016/j.dsr2.2010.05.005>.
- Garcia-Pineda, O., B. Zimmer, M. Howard, W. Pichel, X. Li, and I.R. MacDonald. 2009. Using SAR images to delineate ocean oil slicks with a Texture-Classifying Neural Network Algorithm (TCNNA). *Canadian Journal of Remote Sensing* 35(5):411–421, <http://dx.doi.org/10.5589/m09-035>.
- Gonzalez, R.C., R.E. Woods, and S.L. Eddins. 2004. *Digital Image Processing Using Matlab*. Pearson Prentice-Hall, New Jersey, 609 pp.
- Holt, B. 2004. SAR Imaging of the ocean surface. Pp. 25–80 in *Synthetic Aperture Radar Marine User's Manual*. C. Jackson and J. Apel, eds, US Department of Commerce, NOAA/NESDIS. Available online at: [http://www.sarusersmanual.com/ManualPDF/NOAASARManual\\_CH02\\_pg025-080.pdf](http://www.sarusersmanual.com/ManualPDF/NOAASARManual_CH02_pg025-080.pdf) (accessed August 26, 2013).
- Hu, C., X. Li, W.G. Pichel, and F.E. Muller-Karger. 2009. Detection of natural oil slicks in the NW Gulf of Mexico using MODIS imagery. *Geophysical Research Letters* 36, L01604, <http://dx.doi.org/10.1029/2008GL036119>.
- Hu, C., F. Muller-Karger, C. Taylor, D. Myhre, B. Murch, A.L. Odriozola, and G. Godoy. 2003. MODIS detects oil spills in Lake Maracaibo, Venezuela. *Eos, Transactions, American Geophysical Union* 84(33):313–319, <http://dx.doi.org/10.1029/2003EO330002>.
- Huehnerfuss, H., W. Alpers, W.D. Garrett, P.A. Lange, and S. Stolte. 1983. Attenuation of capillary and gravity waves at sea by monomolecular organic surface films. *Journal of Geophysical Research* 88:9,809–9,816, <http://dx.doi.org/10.1029/JC088iC14p09809>.
- Jackson, C.R., and W. Alpers. 2010. The role of the critical angle in brightness reversals on sunglint images of the sea surface. *Journal of Geophysical Research* 115, C09019, <http://dx.doi.org/10.1029/2009JC006037>.
- Jernelöv, A., and O. Lindén. 1981. IXTOC I: A case study of the world's largest oil spill. *Ambio* 10(6):299–306.
- Knott, E.F., J.F. Shaeffer, and M.T. Tuley. 2004. *Radar Cross Section*, 2<sup>nd</sup> ed. SciTech Publishing, 611 pp.
- Leifer, I., W.J. Lehr, D. Simecek-Beatty, E. Bradley, R. Clark, P. Dennison, Y. Hu, S. Matheson, C.E. Jones, B. Holt, and others. 2012. State of the art satellite and airborne marine oil spill remote sensing: Application to the BP Deepwater Horizon oil spill. *Remote Sensing of Environment* 124:185–209, <http://dx.doi.org/10.1016/j.rse.2012.03.024>.
- Lewis, H.G., and M. Brown. 2001. A generalized confusion matrix for assessing area estimates from remotely sensed data. *International Journal of Remote Sensing* 22(16):3,223–3,235, <http://dx.doi.org/10.1080/01431160152558332>.
- Liu, Y., R.H. Weisberg, C. Hu, and L. Zheng. 2011. Tracking the Deepwater Horizon oil spill: A modeling perspective. *Eos, Transactions, American Geophysical Union* 92(6):45–46, <http://dx.doi.org/10.1029/2011EO060001>.
- MacDonald, I. 2010. Deepwater disaster: How the oil spill estimates got it wrong. *Significance* 7:149–154, <http://dx.doi.org/10.1111/j.1740-9713.2010.00449.x>.
- MacDonald, I., N. Guinasso Jr., S.G. Ackelson, J.F. Amos, R. Duckworth, R. Sassen, and J.M. Brooks. 1993. Natural oil slicks in the Gulf of Mexico visible from space. *Journal of Geophysical Research* 98(C9):16,351–16,364, <http://dx.doi.org/10.1029/93JC01289>.
- Maurizio, M., N. Ferdinando, C.E. Brown, B. Holt, X. Li, W. Pichel, and M. Shimada. 2012. Polarimetric synthetic aperture radar utilized to track oil spills. *Eos, Transactions, American Geophysical Union* 93(16):161–162, <http://dx.doi.org/10.1029/2012EO160001>.
- May, E.F., B.F. Graham, A.S. Chauhan, and R.B. Trengove. 2008. Shear and electrical property measurements of water-in-oil emulsions and implications for multiphase flow meters. *Energy & Fuels* 22:3,308–3,316, <http://dx.doi.org/10.1021/ef800453a>.
- McNutt, M.K., R. Camilli, T.J. Crone, G.D. Guthrie, P.A. Hsieh, T.B. Reyerson, O. Savas, and F. Shaffer. 2011. Review of flow rate estimates of the Deepwater Horizon oil spill. *Proceedings of the National Academy of Sciences of the United States of America*, 109:20,260–20,267, <http://dx.doi.org/10.1073/pnas.1112139108>.
- Mera, D., J.M. Cotos, J. Varela-Pet, and O. Garcia-Pineda. 2012. Adaptive thresholding algorithm based on SAR images and wind data to segment oil spills along the northwest coast of the Iberian Peninsula. *Marine Pollution Bulletin* 64(10):2,090–2,096, <http://dx.doi.org/10.1016/j.marpolbul.2012.07.018>.
- Minchew, B., C.E. Jones, and B. Holt. 2012. Polarimetric analysis of backscatter from the Deepwater Horizon oil spill using L-band synthetic aperture radar. *IEEE Transactions on Geoscience and Remote Sensing* 50(10):3,812–3,830, <http://dx.doi.org/10.1109/TGRS.2012.2185804>.
- Salem, F., and M. Kafatos. 2001. Hyperspectral image analysis for oil spill mitigation. Pp. 748–753 in *Proceedings of ACRS 2001*. 22nd Asian Conference on Remote Sensing, Singapore, November 5–9, 2001 (Trajectory Analysis for Oil Spills).
- Svejkovsky, J., W. Lehr, W. Muskat, G. Graettinger, and J. Mullin. 2012. Operational utilization of aerial multispectral remote sensing during oil spill response: Lessons learned during the Deepwater Horizon (MC-252) spill. *Photogrammetric Engineering & Remote Sensing* 78(10):1,089–1,102.
- Thibodeaux, L.J., K.T. Valsaraj, V.T. John, K.D. Papadopoulos, L.R. Pratt, and N.S. Pesika. 2011. Marine oil fate: Knowledge gaps, basic research, and development needs: A perspective based on the Deepwater Horizon spill. *Environmental Engineering Science* 28(2):87–93, <http://dx.doi.org/10.1089/ees.2010.0276>.
- Topouzelis, K., V. Karathanassi, P. Paviakis, and D. Rokos. 2008. Dark formation detection using neural networks. *International Journal of Remote Sensing* 29(16):4,705–4,720, <http://dx.doi.org/10.1080/01431160801891770>.
- Valenzuela, G. 1978. Theories for the interaction of electromagnetic and ocean waves—A review. *Boundary-Layer Meteorology Journal* 13:61–85, <http://dx.doi.org/10.1007/BF00913863>.
- Xia, Y.Q., and M.C. Boufadel. 2010. Lessons from the Exxon Valdez oil spill disaster in Alaska. *Disaster Advances* 3(4):270–273.